npj | Quantum Information

www.nature.com/npjqi

ARTICLE OPEN

A phononic interface between a superconducting quantum processor and quantum networked spin memories

Tomáš Neuman[1,7], Matt Eichenfield[2,7], Matthew E. Trusheim[1,3,4,7], Lisa Hackett[2], Prineha Narang[1]✉ and Dirk Englund[3,5,6]✉

We introduce a method for high-fidelity quantum state transduction between a superconducting microwave qubit and the ground state spin system of a solid-state artificial atom, mediated via an acoustic bus connected by piezoelectric transducers. Applied to present-day experimental parameters for superconducting circuit qubits and diamond silicon-vacancy centers in an optimized phononic cavity, we estimate quantum state transduction with fidelity exceeding 99% at a MHz-scale bandwidth. By combining the complementary strengths of superconducting circuit quantum computing and artificial atoms, the hybrid architecture provides high-fidelity qubit gates with long-lived quantum memory, high-fidelity measurement, large qubit number, reconfigurable qubit connectivity, and high-fidelity state and gate teleportation through optical quantum networks.

npj Quantum Information (2021)7:121 ; https://doi.org/10.1038/s41534-021-00457-4

INTRODUCTION

Hybrid quantum systems have the potential to optimally combine the unique advantages of disparate physical qubits. In particular, while superconducting (SC) circuits have high-fidelity and high-speed initialization and logic gates[1–8], challenges remain in improving qubit (i) coherence times, (ii) long-range connectivity, (iii) qubit number, and (iv) readout fidelity. A hybrid system may satisfy these challenges by delegating different tasks to constituent physical platforms. Here, we propose an approach to enable such scalable solid-state quantum computing platforms, based fundamentally on a mechanism for high-fidelity qubit transduction between an SC circuit and a solid-state artificial atom (AA). Mediating this transduction is an acoustic bus[9–12] that couples to the SC qubit and an AA electron spin via a combination of piezoelectric transduction and strong spin-strain coupling. Applied to present-day experimental parameters for SC flux qubits and silicon-vacancy (SiV^-) centers in diamond, we estimate quantum state transfer with fidelity exceeding 99% at a MHz-scale bandwidth. Hyperfine coupling to local ^{13}C nuclear-spin qubits enables coherence times exceeding a minute[13], while excited orbital states enable long-distance state transfer across quantum networks by optically heralded entanglement. Moreover, the scheme is extensible to large numbers of spin qubits with deterministic addressability, potentially enabling integration of large-scale quantum memory. Noting that SiV^- single-shot optical readout fidelity has been experimentally demonstrated to exceed 99.9%[14], this approach thus successfully addresses challenges (i-iv). By combining the complementary strengths of SC circuit quantum computing and artificial atoms, this hybrid SC-AA architecture has the essential elements for extensible quantum information processors: a high-fidelity quantum processing unit (QPU), a bus to scalable quantum memory, and a high-fidelity connection long-range optical quantum networks.

Our approach, schematically depicted in Fig. 1, combines four quantum interfaces [QIs, marked as QI1–QI4 in Fig. 1a] between physical modalities: a microwave photon-to-phonon interface, coupling of a phonon to an AA electron spin, coupling of the electron spin to a nuclear spin, and finally coupling of the electron spin to the optical photon. Previous work has investigated these quantum interfaces separately, including the piezoelectric transduction from the microwave circuit to the phonon[12,15–21], spin-strain coupling in solid-state quantum emitters[10,11,22–28], hyperfine interactions of electron spins with nearby nuclei[13,29–33], and spin-dependent optical transitions[34–37]. The last mentioned, optical response of AAs conditioned on the electron spin state, can be used to generate heralded entanglement[14,38,39] and thus allow for networking (e.g., connecting the device to the quantum internet) via quantum-state teleportation. As compared to optomechanical[40–42] and electro-optical[43] transduction schemes, quantum teleportation circumvents the direct conversion of quantum states into photons and thus minimizes the infidelity associated with undetected (unheralded) photon loss. Recent experiments have demonstrated the strain-mediated driving of an AA electron spin ground state with a classical phonon field[44,45]. Using the strain-spin coupling rates measured in those experiments to inform a theoretical model, and introducing a phononic cavity design that achieves the strong coupling regime between a single phonon and an AA spin, we estimate that quantum state transduction is possible with near-unity fidelity, as shown below.

The article is structured as follows. We first develop a general model for phonon-to-spin transduction using a quantum master-equation approach, which we complete by experimentally informed model parameters. After that, we introduce designs for mechanical cavities that achieve strong phonon-spin coupling and efficient quantum state transfer through a combination of high zero-point strain amplitude at AA sites and high expected mechanical quality factors. Based on this we numerically evaluate the master equation describing SC-electron spin transfer and demonstrate a state transfer infidelity below ~1%, and even below 0.1% (sufficient for fault tolerance threshold) using more speculative techniques. Finally, we elaborate using the AA's optical transitions to realize optical interconnects and – by heralded entanglement to other networked quantum memories – to enable

[1]John A. Paulson School of Engineering and Applied Sciences, Harvard University, Cambridge, MA, USA. [2]Sandia National Laboratories, Albuquerque, NM, USA. [3]Massachusetts Institute of Technology, Cambridge, MA, USA. [4]CCDC Army Research Laboratory, Adelphi, MD, USA. [5]Research Laboratory of Electronics, Massachusetts Institute of Technology, Cambridge, MA, USA. [6]Brookhaven National Laboratory, Upton, NY, USA. [7]These authors contributed equally: Tomáš Neuman, Matt Eichenfield, Matthew E. Trusheim. ✉email: prineha@seas.harvard.edu; englund@mit.edu

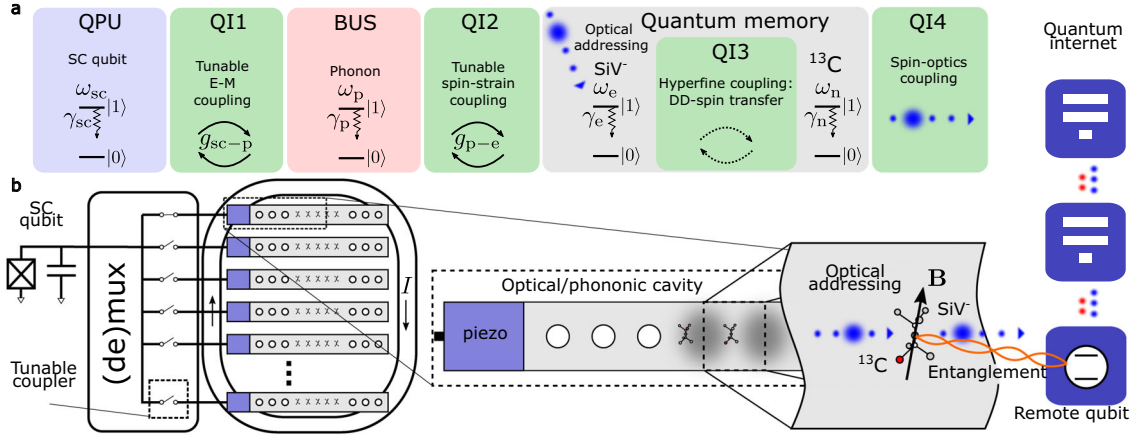

Fig. 1 Quantum memory (QM) and interconnect architecture. a An SC quantum processing unit (QPU) is connected via piezoelectric `quantum interface 1' (QI1) to a phononic BUS. The phonon couples to electronic spin-orbit states of an AA, forming quantum interface 2 (QI2). The AA's fine-structure states can further couple to nuclear-spin to realize a QM via quantum interface 3 (QI3) or they connect to photons in quantum interface 4 (QI4), which finally connects to the quantum internet (blue dots: photonic interconnects). **b** A physical realization of the scheme outlined in **a**. A superconducting qubit is connected via a phononic or microwave multiplexer (mux) to a series of phononic or microwave waveguides that are each interfaced with a mechanical cavity hosting one or many AAs whose electronic fine-structure (spin-orbit) states serve as qubits. The spin-orbit states of each AA interacts with the spin states of a nearby ^{13}C nucleus via the hyperfine interaction, providing ancillae qubits with long coherence times. The AA optical transitions provide an optical interface to quantum networks, for example by multiple attempts of photon-based electron spin entanglement to provide an on-demand entanglement resource. Underlying these capabilities is a transduction scheme that exploits: tunable electro-mechanical (E-M) coupling between the SC qubit and the mechanical mode, tunable spin-strain coupling between the mechanical mode and the electron spin, optical addressing of the electron spin, and hyperfine coupling to connect the electron spin to the nuclear QM.

on-demand, long-range state and gate teleportation with near-unity fidelity.

RESULTS

Theoretical model of the quantum-state transduction

To estimate the state-transfer fidelity we theoretically model the quantum state transfer from the SC qubit to the electron-spin qubit using the quantum-master-equation approach. As in Fig. 1, the SC qubit is directly coupled to a discrete mechanical mode of a phononic cavity via a tunable electromechanical transducer. In Supplementary Note 1 we describe an alternative coupling scheme in which the interaction between the SC qubit and the mechanical mode of the cavity is mediated by guided modes of a microwave[21] or phononic waveguide[12,46]. These guided modes mediate the state transfer between the SC qubit and the discrete phononic mode. The couplings to and out of the waveguide are time-modulated to release ("pitch") and later catch a wavepacket of propagating waveguide modes. Finally, the strain of the mechanical mode interacts with spin levels of the electronic fine-structure states of a diamond AA. By controlling this coupling, the quantum state is transduced to the spin state of the AA electron.

We start our theoretical description from the Hamiltonian schematically depicted in Fig. 1a:

$$\begin{aligned} H_{\mathrm{sc-e}} &= \hbar\omega_{\mathrm{sc}}\sigma_{\mathrm{sc}}^{\dagger}\sigma_{\mathrm{sc}} + \hbar\omega_{\mathrm{p}}b^{\dagger}b + \hbar\omega_{\mathrm{e}}\sigma_{\mathrm{e}}^{\dagger}\sigma_{\mathrm{e}} \\ &\quad + \hbar g_{\mathrm{sc-p}}(t)(\sigma_{\mathrm{sc}}b^{\dagger} + \sigma_{\mathrm{sc}}^{\dagger}b) \\ &\quad + \hbar g_{\mathrm{p-e}}(t)(\sigma_{\mathrm{e}}b^{\dagger} + \sigma_{\mathrm{e}}^{\dagger}b). \end{aligned} \tag{1}$$

Here σ_{sc} ($\sigma_{\mathrm{sc}}^{\dagger}$) is the superconducting qubit two-level lowering (raising) operator, σ_{e} ($\sigma_{\mathrm{e}}^{\dagger}$) is the electron spin lowering (raising) operator, and b ($b^{\dagger}$) is the annihilation (creation) operator of the phonon. The frequencies ω_{sc}, ω_{p}, and ω_{e} correspond to the SC, phonon, and electron-spin excitation, respectively. The SC couples to the phonon mode via the coupling rate $g_{\mathrm{sc-p}}$, and the phonon couples to the electron spin via $g_{\mathrm{p-e}}$. The operators σ_{sc} ($\sigma_{\mathrm{sc}}^{\dagger}$) describe the SC system in a two-level approximation and can be identified with the annihilation (creation) operators of the qubit flux appearing in the circuit cavity-QED description of the device[47,48]. Throughout the paper we assume that all effective couplings in the system are resonant and thus $\omega_{\mathrm{sc}} = \omega_{\mathrm{p}} = \omega_{\mathrm{e}}$.

We consider system losses by adding into the Liouville equation of motion for the density matrix ρ the Lindblad superoperators $\gamma_{c_i}\mathcal{L}_{c_i}(\rho)$:

$$\frac{\mathrm{d}}{\mathrm{d}t}\rho = \frac{1}{\mathrm{i}\hbar}[H_{\mathrm{sc-e}}, \rho] + \sum_i \gamma_{c_i}\mathcal{L}_{c_i}(\rho), \tag{2}$$

where

$$\gamma_{c_i}\mathcal{L}_{c_i}(\rho) = \frac{\gamma_{c_i}}{2}\left(2c_i\rho c_i^{\dagger} - \{c_i^{\dagger}c_i, \rho\}\right), \tag{3}$$

with $c_i \in \{\sigma_{\mathrm{sc}}, b, \sigma_{\mathrm{e}}^{\dagger}\sigma_{\mathrm{e}}\}$, and $\gamma_{c_i} \in \{\gamma_{\mathrm{sc}}, \gamma_{\mathrm{p}}, \gamma_{\mathrm{e}}\}$ representing the decay (decoherence) rates of the respective excitations. We note that the Lindblad superoperators $\mathcal{L}_{\sigma_{\mathrm{sc}}}(\rho)$ and $\mathcal{L}_b(\rho)$ describe the T_1 processes including the qubit decay, whereas $\mathcal{L}_{\sigma_{\mathrm{e}}^{\dagger}\sigma_{\mathrm{e}}}(\rho)$ describes pure dephasing of the electron spin (a T_2 process) considering the long-lived character of the spin excitation. We do not include pure dephasing (T_2) processes of the SC qubit and the mechanical mode, but consider rates of the T_1 processes corresponding to the experimentally achievable T_2 times (since $T_1 \sim T_2$ for phonons and SC qubits). We do not include thermal occupation of modes as we consider the system to be cooled to ~mK temperatures. While we assume that the system is in thermal equilibrium with the dilution refrigerator bath, it has been observed in certain systems that non-equilibrium excitations can occur[49,50]–perhaps from stray infrared photons. For simplicity, we ignore these non-equilibrium excitations but note that they could potentially complicate the dynamics if they cannot be eliminated.

For high-fidelity state transfer without coherent reflections, it is necessary to switch the magnitude of the Jaynes-Cummings couplings $g_{\mathrm{p-e}}$ and $g_{\mathrm{sc-p}}$ in a sequence that allows for step-wise transfer of the quantum state to the mechanical mode and finally to the electron spin. To that end, we first switch on the coupling $g_{\mathrm{sc-p}}$ between the SC qubit and the mechanical mode while turning off the phonon-electron-spin coupling $g_{\mathrm{p-e}}$. After completing the state transfer to the mechanical mode, we switch off $g_{\mathrm{sc-p}}$ and apply a state-transfer pulse $g_{\mathrm{e-p}}$ completing the

procedure. Each of the pulses represents a SWAP gate (up to a local phase), so the state-transfer protocol can be inverted by interchanging the pulse order. In particular, we assume that each coupling has a smooth time dependence given by

$$g_{\text{sc-p}}(t) = g_{\text{scp}}\ \text{sech}(2g_{\text{scp}}[t-\tau_{\text{scp}}]) \tag{4}$$

$$g_{\text{p-e}}(t) = g_{\text{pe}}\ \text{sech}(2g_{\text{pe}}[t-\tau_{\text{pe}}]), \tag{5}$$

where g_{scp}, g_{pe} are time-independent amplitudes and τ_{scp}, τ_{pe} are time delays of the respective pulses. We choose the smoothly varying pulses over rectangular pulses to account for the bandwidth-limitation of experimentally achievable time-dependent couplings. In our simulations we adjust $\Delta\tau_{\text{sc-p-e}} = \tau_{\text{pe}} - \tau_{\text{scp}}$ to optimize the state-transfer fidelity $\mathcal{F}$ defined as:

$$\mathcal{F} = \left|\text{Tr}\left\{\sqrt{\sqrt{\rho_{\text{i}}}\rho_{\text{f}}\sqrt{\rho_{\text{i}}}}\right\}\right|, \tag{6}$$

where ρ_{i} (ρ_{f}) is the density matrix of the initial state of the SC qubit (final state stored in the electron spin). Due to the finite simulation time we further approximate the ideal infinite time spread of the applied pulses and apply the pulses at a sufficient delay after the start of the simulation.

Physical transducer parameterization

The values of the coupling and loss parameters govern the system performance. Coupling rates between a microwave (MW) resonator and a phononic cavity[21] up to ~100 MHz have been predicted in an MW-cavity resonantly coupled to a discrete phononic mode via a piezoelectric coupler. Optimizing the coupling requires matching the MW line impedance with the phonon waveguide impedance[51]. For tunable coupling between the SC qubit and the mechanical mode of the cavity, the MW resonator can be substituted by the SC qubit itself as in a recent experimental demonstration[12]. Using an additional Josephson junction with externally controllable flux as a tunable microwave switch mated[12,52–54] to the piezoelectric coupler additionally enables controllable time-varying coupling between the SC qubit and the phonon. Based on recent experiments[12,55,56], we assume that the coupling between the SC qubit and the mechanical mode can reach up to $g_{\text{scp}}/(2\pi) = 10$ MHz. We conservatively assume SC qubit coherence times on the order of microseconds ($\gamma_{\text{sc}}/(2\pi) =$ 10 kHz), while best-case SC coherence times approach milliseconds[8].

We consider that the spin qubit is formed by the two low-energy fine-structure states of the SiV^- as described in Supplementary Note 2 These two states have distinct orbital and spin character which impedes direct coupling of the spin-qubit transition to either strain or magnetic fields. Generally, a combination of applied strain and magnetic field is thus necessary to address the SiV^- spin qubit. We thus control the spin-strain coupling via locally applied time-dependent magnetic fields to realize the effective controllable Jaynes-Cummings interaction introduced in Eq. (5). Several strategies have been devised to engineer the effective spin-strain coupling[27,57] that generally rely on the application of externally controllable time-dependent magnetic fields and pulsed optical drives as we detail in Supplementary Note 2. All of these approaches are perturbative in character and the maximum achievable value of the resulting effective spin-strain coupling g_{pe} is therefore decreased with respect to the bare strain coupling measured for fine-structure spin-allowed transitions g_{orb} to $g_{\text{pe}} \approx 0.1 g_{\text{orb}}$. The spin-strain interaction of group-IV quantum emitters in diamond has been measured at 1 PHz/strain[57]. We estimate that for an efficient state transfer between the mechanical mode and the electron-spin states, the spin-mechanical coupling g_{orb} would need to reach a value of approximately $g_{\text{orb}}/(2\pi) \approx 10$ MHz (leading to the effective phonon-electron-spin $g_{\text{pe}}/(2\pi) \approx 1$ MHz). To that end, a mechanical resonance with zero-point strain of $\sim 10^{-9} - 10^{-8}$ and a high quality factor is needed. We now design (opto-)mechanical cavities that fulfill both of these requirements.

Realization of cavity for strong phonon-spin coupling

This section introduces a mechanical cavity that allows fast and efficient phonon-mediated quantum-state transduction to and from the electron spin. We model the cavities through a series of finite-element numerical simulations[58,59] (performed using COMSOL Multiphysics[60]) of the mechanical resonance within the continuum description of elasticity. These simulations use adiabatic absorbing layers at the boundaries[61]. We obtain the optical response of the diamond cavity from a solution of Maxwell's equations in the materials described via their linear-response dielectric function.

We describe two architectures of high-Q mechanical cavities whose zero-point strain field gives rise to the phonon-spin strong coupling required in the transduction scheme. (i) The first design is a silicon cavity with a thin (100 nm) layer of diamond heterogeneously integrated to the silicon substrate [shown in Fig. 2]. This takes advantage of mature design and fabrication of silicon nanophononics[58,62,63], exceptionally small decoherence rates of microwave frequency phonons in suspended single-crystal silicon[64], and new techniques in heterogeneous integration of diamond nanoscale membranes[65,66]. (ii) The second design is an all-diamond optomechanical cavity that at the same time supports an optical and phononic mode for mechanical and optical addressing of the electron spin [shown in Fig. 3]. As depicted in Fig. 2a, the silicon cavity is embedded in a phononic crystal to minimize the cavity loss; it is also weakly coupled to a phononic waveguide that mediates the interaction of the cavity with the SC circuit. Simultaneous acoustic and microwave electrical impedance matching has been demonstrated[51,67] to such wavelength-scale structures using thin piezoelectric films, enabling coupling into the waveguide from the superconducting system with low insertion loss. The cavity is separated from the waveguide by a series of barrier holes to allow tuning the coupling rate between the discrete cavity mode and the guided phonons. Figure 2b details this cavity. The silicon platform forming the base of the cavity is covered with a thin layer (100 nm) of diamond hosting the defects.

To analyze the cavity mechanical properties, we calculate the distribution of the elastic energy density of a mechanical mode of the cavity resonant at $\omega_{\text{p}}/(2\pi) = 2.0$ GHz. The energy density is concentrated in the thin constriction formed by the diamond layer for efficient phonon-spin coupling. Figure 2d shows the calculated bare phonon-spin coupling $g_{\text{orb}} = (\epsilon_{xx} - \epsilon_{yy})d$ corresponding to the strain field in the ground state of the resonator–the zero-point strain. Here $d \approx 1$ PHz/strain is the strain susceptibility of the defect electron spin, and ϵ_{xx} (ϵ_{yy}) are the components of the zero-point strain expressed in the coordinate system of the defect (see Supplementary Note 3). As we show in Fig. 2d, $g_{\text{orb}}/(2\pi)$ reaches up to 5.4 MHz and we thus estimate the effective coupling $g_{\text{pe}}/(2\pi) \approx 0.5$ MHz. An equally important figure of merit characterizing the cavity performance is the cavity coupling to the waveguide modes. The distribution of the mechanical energy flux in the cavity in Fig. 2e shows that the cavity mode interacts with the waveguide modes, introducing a decay rate κ_{p} of the cavity mode. Figure 2f plots κ_{p} as a function of the number of barrier holes on a logarithmic scale. Thus, κ_{p} decreases exponentially with the number of separating barrier holes from almost $\sim 10^7$ Hz to ~1 Hz for seven holes. For larger number of holes, the cavity lifetime becomes practically limited by the intrinsic material properties of silicon and diamond and could be as low as ~0.1 Hz[64] assuming no additional loss due to the introduction of the diamond nanomembrane.

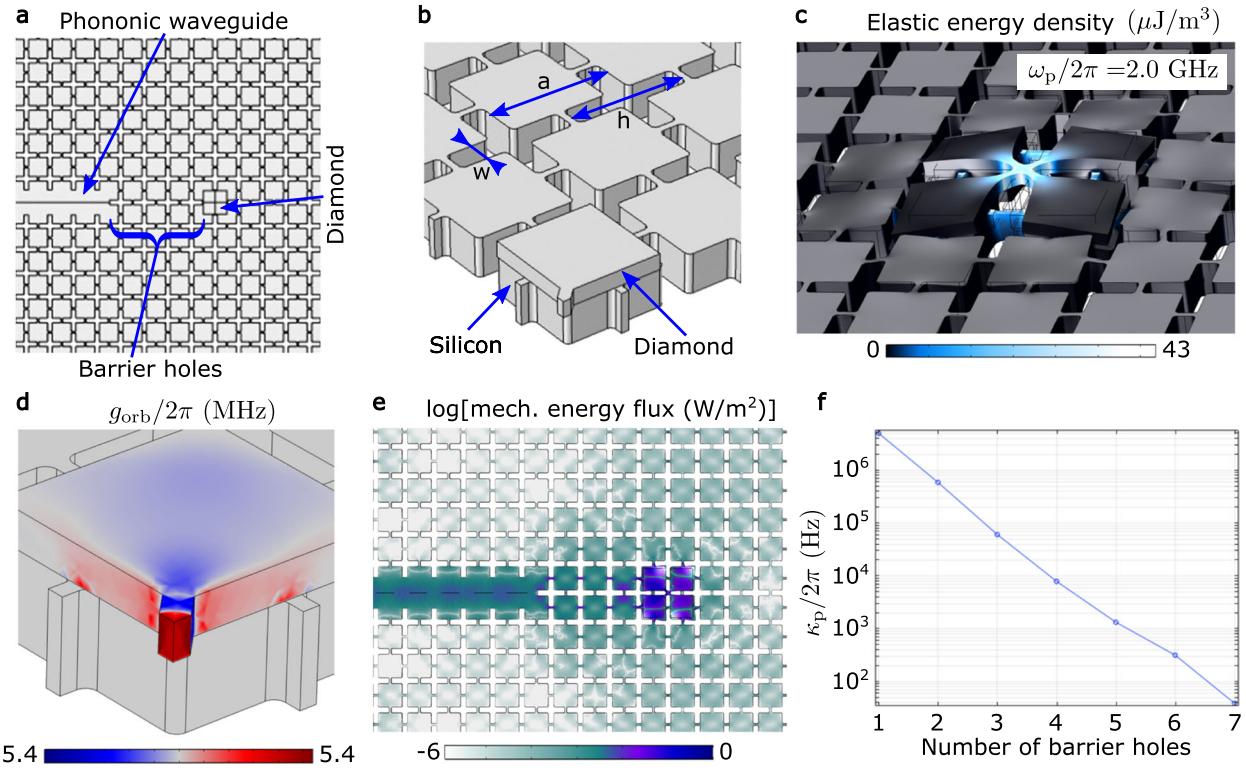

Fig. 2 Silicon phononic cavity. a A mechanical resonator embedded in a phononic crystal is separated from a phononic waveguide by a number of barrier holes. It is capped by a thin diamond layer placed over the silicon layer. **b** A close-up of one quarter of the silicon-diamond structure with dimensions $a = 800$ nm, $h = 0.94a$, and $w = 0.2a$. The silicon (diamond) layer thickness is $t_{Si} = 250$ nm ($t_D = 100$ nm). The width of the thin rectangular diamond interconnects is $w_D = 70$ nm. **c** The elastic energy density of the cavity mode is concentrated in the thin constriction of the diamond layer. The geometry of the cavity is artificially distorted along the coordinate of the mechanical mode. **d** The coupling rate between the mechanical mode and the electron spin calculated as $g_{orb} \approx (\epsilon_{xx} - \epsilon_{yy})d$, with $d \approx 1$ PHz/strain being the strain susceptibility of SiV^- defect. **e** The mechanical energy flux of the combined eigenmode of the mechanical cavity and the waveguide. **f** Mechanical damping κ_p of the phononic cavity as a function of the number of barrier holes separating it from the phononic waveguide.

Figure 3 shows the all-diamond optomechanical cavity, which consists of a diamond beam with an array of elliptical holes of varying sizes. The hole array simultaneously produces a phononic and photonic cavity that concentrates both the mechanical strain of the phononic mode and the optical electric field of the electromagnetic mode on the AA in the cavity center. The distribution of the elastic energy density of a phononic mode of frequency $\omega_p/(2\pi) = 17.2$ GHz shown in Fig. 3a reveals that the mechanical energy is dominantly concentrated around the center of the beam. Using the calculated values of zero-point strain of this mode we calculate the achievable bare coupling strength g_{orb} and show the result in Fig. 3b. The maximal achievable effective phonon-spin qubit coupling in the diamond cavity thus reaches up to $g_{pe}/(2\pi) \approx 0.1 g_{orb}/(2\pi) = 2.4$ MHz. This diamond cavity furthermore offers the possibility to increase the efficiency of optical addressing of the diamond AAs by concentrating light of a vacuum wavelength $\lambda_{opt} = 732$ nm into an optical mode that is spatially overlapping with the cavity mechanical mode. The high calculated optical quality factor $Q_{opt} = 10^6$ can be used to increase the efficiency of optical addressing of the diamond AA.

In summary, we have designed (opto)mechanical cavities that sustain mechanical modes whose zero-point strain fluctuations enable *strong coupling* between an AA spin and a single quantum of mechanical motion. The feasibility of such devices marks an important practical step towards transducers relying on spin-strain interactions. Having established the achievable values of couplings and decay rates governing the dynamics of the system, we now proceed to analyze the numerical results of our quantum-sate transduction protocol.

Numerical analysis of SC-emitter quantum state transfer

Mechanical resonators of high-quality factors exceeding $Q \sim 10^7$ have been demonstrated experimentally[64]. The limiting time-scale for high-fidelity state transfer is therefore the decoherence of the SC and electron spin qubits, so it is necessary to transfer the SC population rapidly into the phononic mode. The long-lived phonon then allows transduction into the AA electron spin levels of the emitter, where the qubit can be addressed optically, or is further transferred to the quantum memory - the nuclear spin[13,33]. We numerically evaluate the master equation, and show the results of the time evolution of such a system in Fig. 4a. In our simulation we consider $g_{scp}/(2\pi) = 10$ MHz, $g_{pe}/(2\pi) = 1$ MHz, $\gamma_{sc}/(2\pi) = 1.66 \times 10^{-5}$ GHz[7,8], $\gamma_p/(2\pi) = 10^{-7}$ GHz, $\gamma_e/(2\pi) = 10^{-5}$ GHz. The SC qubit is initialized in the excited state while the rest of the system is considered to be in the ground state. We let the system evolve in time and apply the series of control pulses [Eqs. (4) and (5) shown in Fig. 4b as a blue line and a red dashed line, respectively] to transfer the initial population of the SC qubit (full blue line) sequentially to the phonon (red dashed line), and the electron spin (black dash-dotted line), as shown in Fig. 4a.

To further analyze the transduction we calculate the state-transfer fidelity $\mathcal{F}$ defined in Eq. (6) as a function of the phonon-spin coupling g_{pe} and the electron-spin dephasing rate γ_e. We vary $g_{pe}/(2\pi)$ in the range from 100 kHz, representing a conservative estimate of the phonon-spin coupling rate, to 10 MHz which exceeds the value we estimate for the silicon phononic cavity by an order of magnitude. The role of the electron-spin coherence on the overall state-transfer fidelity [together with the infidelity $\log(1 - \mathcal{F})$] is shown in Fig. 4c [Fig. 4d] assuming $\gamma_p/(2\pi) = 10^{-7}$ GHz, i.e., we consider a high-quality resonance of the phononic

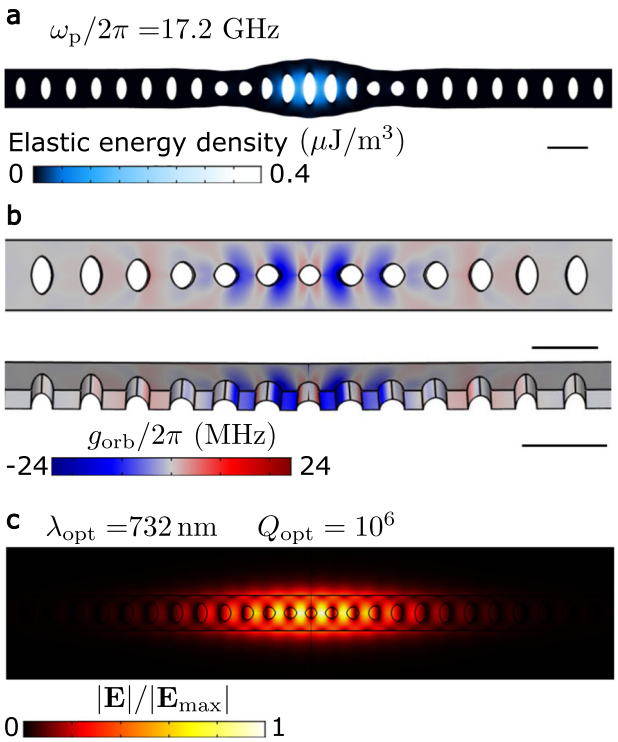

Fig. 3 Diamond optomechanical cavity. a Distribution of elastic energy density of a mode of the diamond cavity resonant at $\omega_p/(2\pi) = 2$ GHz. The cavity geometry is artificially distorted along the coordinate of the mechanical mode for emphasis. The energy density is concentrated in the central part of the cavity. **b** Calculated coupling rate g_{orb} in the phononic cavity. **c** Normalized amplitude of the optical electric field at vacuum wavelength $\lambda_{opt} = 732$ nm of an optical mode of the diamond cavity of an optical quality factor $Q_{opt} \approx 10^6$. The electric field is concentrated around the center of the cavity and thus overlaps with the regions providing high values of g_{orb}. Scale bars: (**a**) 350 nm, (**b**) 350 nm (top), and 500 nm (bottom).

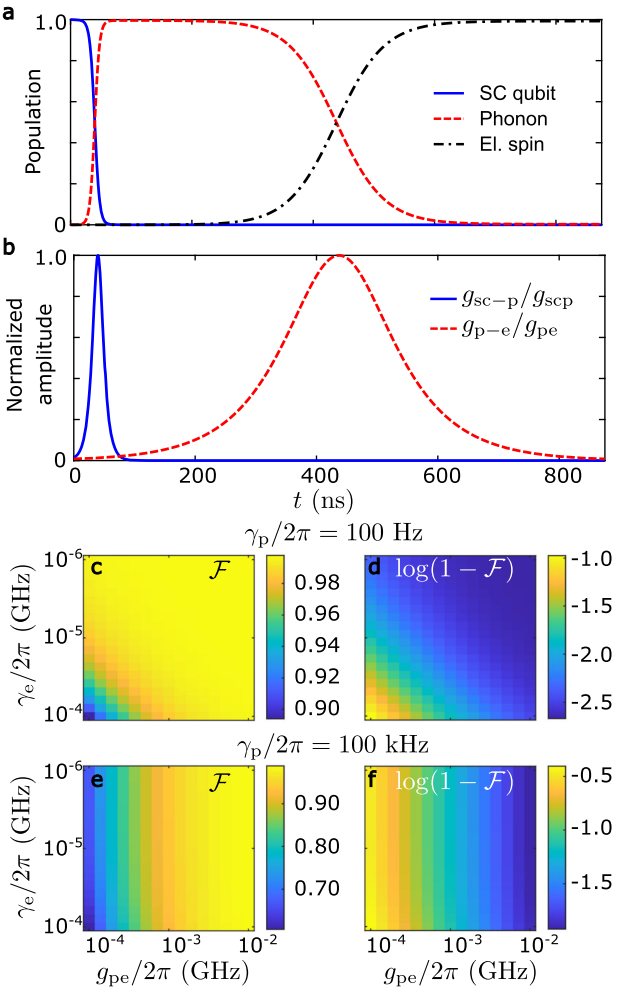

Fig. 4 State transfer from the SC qubit to the electron spin. The system begins in the excited state of the SC qubit, then evolves according to the master equation Eq. (2). The time-dependent populations of the SC qubit (full blue), the cavity phonon (red dashed), and the electron spin qubit (black dash-dotted) are plotted as a function of time in **a**. After initializing the system, we apply the series of pulses shown in **b**, as described in the text, and let the system evolve until the state is transferred to the electron spin. **c**, **e** The state-transfer fidelity $\mathcal{F}$, and **d**, **f** $\log(1-\mathcal{F})$. Both $\mathcal{F}$, and $\log(1-\mathcal{F})$ are calculated as a function of the phonon-electron-spin coupling g_{pe} and the electron-spin dephasing rate γ_e. We maximize $\mathcal{F}$ for each pair of parameters [γ_e, g_{pe}] by adjusting the delays between the respective pulses applied to drive the system dynamics. We consider (**c**, **d**) $\gamma_p/(2\pi) = 10^{-7}$ GHz (corresponding to the mechanical quality factor $Q \sim 10^7$) and (**e**, **f**) $\gamma_p/(2\pi) = 10^{-4}$ GHz in the calculations.

cavity, and in Fig. 4e [Fig. 4f] for a bad phononic cavity using $\gamma_p/(2\pi) = 10^{-4}$ GHz. We consider $\gamma_e/(2\pi) = 10^{-4}$ GHz as a conservative upper bound of the electron-spin decoherence rate. However, progress in quantum technology indicates that the lower value considered in our calculations, $\gamma_e/(2\pi) = 10^{-6}$ GHz, can be achieved in state-of-the-art systems[57]. Our calculation shows that for high transfer fidelity (infidelity of less than ~1%) high-quality phononic cavity is required and the electron-spin decoherence rate should not exceed $\gamma_e/(2\pi) \approx 10^{-5}$ GHz, well within the experimentally accessible range. This indicates that electro-mechanical state transfer is potentially achievable in present systems. The calculations of the state-transfer fidelity (infidelity) assuming a bad phononic cavity in Fig. 4e [Fig. 4f] demonstrate the importance of high phonon-spin coupling rate to optimize the state-transfer fidelity.

Quantum interfacing

The AA electron-spin qubit serves as the network bus, mediating coupling to not just phonons as well as photons and nuclear spins. In particular, the spin-dependent optical transitions enable photon-mediated coupling of the quantum device to, for example, distant quantum memories in a quantum network, as illustrated in Fig. 1a. One approach would be to perform spin-to-photon conversion by optically addressing the electron spin after the SC qubit has been transduced to it. This could be performed via a variety of spin-photon interfacing procedures, including direct optical excitation of the quantum emitter[68], or a spin-photon controlled-phase gate mediated by a cavity mode. However, the fidelity of this approach is intrinsically limited by the achievable emitter-cavity cooperativity and the detuning between spin states. In particular, current experiments have demonstrated entanglement fidelities of 0.94 and heralding efficiencies of 0.45[14]. The photon loss associated with this direct spin-to-photon transduction also destroys the quantum state that was to be transported.

An alternative approach transmits the superconducting qubit with near-unity efficiency and fidelity, using deterministic state teleportation to a distant target qubit in a quantum network. In this approach, a ^{13}C nuclear spin, hyperfine coupled to the SiV electron spin, is entangled with the quantum network target qubit by repeat-until-success optical heralding[14,34,38,39]. The SC qubit is then transduced into the SiV electron spin system by the procedure described above. Finally, a Bell-state measurement of

the nuclear and electron spins followed by a feed-forward single-qubit gate completes the teleportation of the nuclear spin qubit to the quantum network target. This scheme never transduces the SC qubit to the optical domain and thus avoids photon transmission losses. Instead, electron-nuclear spin gates can be used to teleport the qubit across a quantum network. This second approach can achieve near-unity state-transfer fidelity and efficiency provided that entangled qubit pairs shared between nodes of the quantum network can be prepared on demand. This preparation of on-demand entanglement has been recently realized for diamond NV centers[38] with spin-spin teleportation fidelities reaching up to 0.84[38,69]. Ongoing experimental and theoretical advances promise to enable near-unity teleportation fidelity, including through environmentally insensitive quantum emitters (such as the SiV considered in this work) and entanglement schemes to improve noise and error resilience.

The hyperfine interactions of the electron spin with nearby spins of nuclear isotopes is often an unwanted source of electron-spin decoherence hindering the ability to maintain and control the electron-spin qubits over long time scales. Dynamical decoupling techniques[29,70] have been applied to mitigate this decoherence and reach ~1 ms to ~10 ms coherence times in SiV systems[68,71,72]. However, recent theoretical and experimental work shows that the nuclear spins can be used as a resource as their quantum state can be selectively addressed and controlled via the quantum state of the electron spin itself[13,31,32] with high fidelity. Combined with the extraordinarily long (exceeding ~1 s) coherence times of these nuclear spins, it has been proposed that the nuclear-spin bath could serve as a quantum register[13,31,33] and could store quantum states and thus serve as a QM. In Supplementary Note 4 we describe how the protocol developed in[13] can implement a quantum SWAP gate allowing for state transfer from the electron-spin qubit to a single nuclear spin of a nearby ^{13}C atom. Assuming electron-spin pure dephasing of $\gamma_e/(2\pi) = 10$ kHz, nuclear-spin pure dephasing of $\gamma_n/(2\pi) = 1$ Hz, a moderate electron-spin hyperfine coupling $A_{\|} = 500$ kHz, and a conservative value of an external microwave drive Rabi frequency $\Omega_{mw}/(2\pi) \approx 3.9$ kHz, we estimate that the state-transfer fidelity $\mathcal{F}_{en}$ of this process could reach $\mathcal{F}_{en} \approx 0.9975$.

The compactness of this diamond QM further opens up the possibility to scale the system. Using a mechanical or microwave switching network, each SC qubit could be selectively coupled to a large number of mechanical cavities depending on the experimental architecture. As each additional coupled cavity introduces a decay channel, low-loss high-isolation switching is required. As an example, we consider a pitch-and-catch scheme could [Supplementary Note 1 wherein the quantum state is launched into a mechanical waveguide with controllable coupling to many phononic resonators. For high fidelity state transfer $\mathcal{F} > 0.99$, the total insertion loss of all switches must remain below 0.04 dB, which may prove experimentally challenging. Considering experimentally achievable AA densities, we estimate that about 10 AAs could be individually addressed within the mechanical mode volume of ~10^7 nm^3 of each waveguide. These can be individually optically addressed due to their inhomogeneous optical and microwave transition distribution[73,74], induced by natural variations in local static strain within the diamond crystal.

Each color center enables high-fidelity coupling to ~10 nuclear spins[13]. Allowing for, say, 10 parallel QM interconnects from the QPU would thus provide a total QM capacity of about $\sim 10 \times 10 \times 10 =$ kqubits. Introducing spatial multiplexing (e.g., using microwave switches) would multiply the QM capacity further.

As we show in Supplementary Note 5, the proposed architecture coupling a large number of electron-spin qubits to a shared mechanical mode further opens the opportunity for efficient phonon-mediated spin-entangling quantum gates[10,11,75,76]. These gates enable preparation of highly entangled many-spin states, such as the Greenberger-Horne-Zeilinger (GHZ) state, that can serve as resources for further quantum-state manipulation. Specifically, an N-electron-spin GHZ state coupled to the same phononic cavity could increase the phase sensitivity to strain N-fold[77]. Thus, a GHZ state prepared in advance of the SC-to-spin transduction would speed up the controlled-phase gates, N times speedup for a N–spin GHZ state. Combined with local gates acting on the spins and the phonon, a GHZ state could be used to boost the speed and fidelity of the SWAP gate.

DISCUSSION

We introduced an architecture for high-bandwidth, high-fidelity quantum state transduction between superconducting microwave AA spin qubits at rates far exceeding intrinsic system decay and decoherence. The resulting hybrid architecture combines the favorable attributes of quantum memories with SC quantum information processors, enabling a wide range of functionalities currently unavailable to a stand-alone superconducting or spin-based architectures.

Strong coupling of a single defect center spin to a high-quality mechanical cavity, the key element of our proposal, remains to be experimentally demonstrated. Nevertheless, our analysis shows experimental feasibility of the proposal in state-of-the-art mechanical systems. Further experimental challenges exist in the demonstrations of controllable electro-mechanical and mechanical-mechanical couplers that are necessary for the cascaded state transfer. Rapid development of micro-mechanical systems indicates that the above-mentioned experimental challenges can be solved in the foreseeable future.

Looking further ahead, reaching fault-tolerant quantum information processing will likely require gate and measurement errors below 0.1%. Fortunately, there appear to be several avenues to speed up, and thus improve, the fidelity of quantum state transfer between phonon to spin encoding. These include further strain concentration (e.g., through thinner diamond patterning), identifying different AAs with increased strain coupling, state distillation, and the use of pre-prepared spin GHZ states—and to that end, fast and reliable spin-entangling protocols must be developed both theoretically and experimentally. Thus, a GHZ state prepared in advance of the SC-to-spin transduction would speed up the controlled-phase gates by N times for a N-spin GHZ state. The use of a GHZ-spin state benefits only if its decoherence rate, which is N times faster than the single-spin decoherence rate γ_e, is much slower than the phonon decoherence rate, i.e., $N\gamma_e \gg \gamma_p$. With coherence times of color center spins already exceeding one minute for the NV-diamond system and expected to be very long also for group-IV vacancy centers at low enough temperature where phonon-mediated dephasing between the ground state orbitals is quenched, this regime may soon become accessible. Then, combined with local gates acting on the spins and the phonon, a GHZ state could significantly boost the speed and fidelity of the SWAP gate.

To summarize our key results, the SC-AA hybrid architecture combines the complementary strengths of SC circuit quantum computing and artificial atoms, realizing the essential elements of an extensible quantum information processing architecture. There are, of course, components that need to be realized and assembled into one system, which will diminish certain performance metrics, at least near-term. Nonetheless, even our basic performance considerations show that these different capabilities – QPU, QM, bus, and quantum network port – should leverage distinct physical modalities in a hybrid system, much like a classical computing system.

METHODS

We solve the quantum master equation using a custom code implemented in Matlab[78] following ref. [79]. The finite-element simulations have been

performed using COMSOL Multiphysic[60]. The finite-element simulations implement adiabatic absorbing layers as absorbing boundary conditions[61]. The elastodynamics of the structure are obtained by solving the elastic wave equation for the particle displacement of the material. The materials were described in the continuum limit by their elastic properties.

DATA AVAILABILITY

Data are available upon reasonable request.

Received: 17 May 2020; Accepted: 26 May 2021;
Published online: 04 August 2021

REFERENCES

1. Neeley, M. et al. Generation of three-qubit entangled states using superconducting phase qubits. *Nature* **467**, 570 (2010).
2. Pop, I. M., Geerlings, K., Catelani, G., Schoelkopf, R. J., Glazman, L. I. & Devoret, M. H. Coherent suppression of electromagnetic dissipation due to superconducting quasiparticles. *Nature* **508**, 369 (2014).
3. Ofek, N. et al. Extending the lifetime of a quantum bit with error correction in superconducting circuits. *Nature* **536**, 441 (2016).
4. Narla, A. et al. Robust concurrent remote entanglement between two superconducting qubits. *Phys. Rev. X* **6**, 031036 (2016).
5. Lu, Y. et al. Universal stabilization of a parametrically coupled qubit. *Phys. Rev. Lett.* **119**, 150502 (2017).
6. Barends, R. et al. Diabatic gates for frequency-tunable superconducting qubits. *Phys. Rev. Lett.* **123**, 210501 (2019).
7. Arute, F. et al. Quantum supremacy using a programmable superconducting processor. *Nature* **574**, 505 (2019).
8. Kjaergaard, M. et al. Superconducting qubits: current state of play. *Annu. Rev. Condens. Matter Phys.* **11**, null (2020).
9. Chu, Y. et al. Quantum acoustics with superconducting qubits. *Science* **358**, 199 (2017).
10. Kuzyk, M. C. & Wang, H. Scaling phononic quantum networks of solid-state spins with closed mechanical subsystems. *Phys. Rev. X* **8**, 041027 (2018).
11. Li, X., Kuzyk, M. C. & Wang, H. Honeycomblike phononic networks of spins with closed mechanical subsystems. *Phys. Rev. Appl.* **11**, 064037 (2019).
12. Bienfait, A. et al. Phonon-mediated quantum state transfer and remote qubit entanglement. *Science* **364**, 368 (2019).
13. Bradley, C. E. et al. A ten-qubit solid-state spin register with quantum memory up to one minute. *Phys. Rev. X* **9**, 031045 (2019).
14. Bhaskar, M. K. et al. Experimental demonstration of memory-enhanced quantum communication. *Nature* **580**, 60 (2020).
15. Schuetz, M. J. A., Kessler, E. M., Giedke, G., Vandersypen, L. M. K., Lukin, M. D. & Cirac, J. I. Universal quantum transducers based on surface acoustic waves. *Phys. Rev. X* **5**, 031031 (2015).
16. Manenti, R. et al. Circuit quantum acoustodynamics with surface acoustic waves. *Nat. Commun.* **8**, 975 (2017).
17. Arrangoiz-Arriola, P., Wollack, E. A., Pechal, M., Witmer, J. D., Hill, J. T. & Safavi-Naeini, A. H. Coupling a superconducting quantum circuit to a phononic crystal defect cavity. *Phys. Rev. X* **8**, 031007 (2018).
18. Hann, C. T. et al. Hardware-efficient quantum random access memory with hybrid quantum acoustic systems. *Phys. Rev. Lett.* **123**, 250501 (2019).
19. Higginbotham, A. P. et al. Harnessing electro-optic correlations in an efficient mechanical converter. *Nat. Phys.* **14**, 1038 (2018).
20. Sletten, L. R., Moores, B. A., Viennot, J. J. & Lehnert, K. W. Resolving phonon fock states in a multimode cavity with a double-slit qubit. *Phys. Rev. X* **9**, 021056 (2019).
21. Wu, M., Zeuthen, E., Balram, K. C. & Srinivasan, K. Microwave-to-optical transduction using a mechanical supermode for coupling piezoelectric and optomechanical resonators. *Phys. Rev. Appl.* **13**, 014027 (2020).
22. Falk, A. L. et al. Electrically and mechanically tunable electron spins in silicon carbide color centers. *Phys. Rev. Lett.* **112**, 187601 (2014).
23. Golter, D. A., Oo, T., Amezcua, M., Stewart, K. A. & Wang, H. Optomechanical quantum control of a nitrogen-vacancy center in diamond. *Phys. Rev. Lett.* **116**, 143602 (2016).
24. Lemonde, M.-A. et al. Phonon networks with silicon-vacancy centers in diamond waveguides. *Phys. Rev. Lett.* **120**, 213603 (2018).
25. Chen, H. Y., MacQuarrie, E. R. & Fuchs, G. D. Orbital state manipulation of a diamond nitrogen-vacancy center using a mechanical resonator. *Phys. Rev. Lett.* **120**, 167401 (2018).
26. Maity, S. et al. Spectral alignment of single-photon emitters in diamond using strain gradient. *Phys. Rev. Applied* **10**, 024050 (2018).
27. Meesala, S. et al. Strain engineering of the silicon-vacancy center in diamond. *Phys. Rev. B* **97**, 205444 (2018).
28. Udvarhelyi, P., Shkolnikov, V. O., Gali, A., Burkard, G. & Pályi, A. Spin-strain interaction in nitrogen-vacancy centers in diamond. *Phys. Rev. B* **98**, 075201 (2018).
29. De Lange, G., Wang, Z., Riste, D., Dobrovitski, V. & Hanson, R. Universal dynamical decoupling of a single solid-state spin from a spin bath. *Science* **330**, 60 (2010).
30. Childress, L. et al. Coherent dynamics of coupled electron and nuclear spin qubits in diamond. *Science* **314**, 281 (2006).
31. Taminiau, T. H., Cramer, J., van der Sar, T., Dobrovitski, V. V. & Hanson, R. Universal control and error correction in multi-qubit spin registers in diamond. *Nat. Nanotechnol.* **9**, 171 (2014).
32. Waldherr, G. et al. Quantum error correction in a solid-state hybrid spin register. *Nature* **506**, 204 (2014).
33. Nguyen, C. T. et al. Quantum network nodes based on diamond qubits with an efficient nanophotonic interface. *Phys. Rev. Lett.* **123**, 183602 (2019a).
34. Pfaff, W. et al. Unconditional quantum teleportation between distant solid-state quantum bits. *Science* **345**, 532 (2014).
35. Bernien, H. et al. Heralded entanglement between solid-state qubits separated by three metres. *Nature* **497**, 86 (2013).
36. Evans, R. E. et al. Photon-mediated interactions between quantum emitters in a diamond nanocavity. *Science* **362**, 662 (2018).
37. Awschalom, D. D., Hanson, R., Wrachtrup, J. & Zhou, B. B. Quantum technologies with optically interfaced solid-state spins. *Nat. Photonics* **12**, 516 (2018).
38. Humphreys, P. C. et al. Deterministic delivery of remote entanglement on a quantum network. *Nature* **558**, 268 (2018).
39. Rozpedek, F. et al. Near-term quantum-repeater experiments with nitrogen-vacancy centers: overcoming the limitations of direct transmission. *Phys. Rev. A* **99**, 052330 (2019).
40. Stannigel, K., Rabl, P., Sørensen, A. S., Zoller, P. & Lukin, M. D. Optomechanical transducers for long-distance quantum communication. *Phys. Rev. Lett.* **105**, 220501 (2010).
41. Stannigel, K., Rabl, P., Sørensen, A. S., Lukin, M. D. & Zoller, P. Optomechanical transducers for quantum-information processing. *Phys. Rev. A* **84**, 042341 (2011).
42. Bochmann, J., Vainsencher, A., Awschalom, D. D. & Cleland, A. N. Nanomechanical coupling between microwave and optical photons. *Nat. Phys.* **9**, 712 (2013).
43. Rueda, A. et al. Efficient microwave to optical photon conversion: an electro-optical realization. *Optica* **3**, 597 (2016).
44. Whiteley, S. J. et al. Spin–phonon interactions in silicon carbide addressed by gaussian acoustics. *Nat. Phys.* **15**, 490 (2019).
45. Maity, S. et al. Coherent acoustic control of a single silicon vacancy spin in diamond. *Nat. Commun.* **11**, 193 (2020).
46. Fang, K., Matheny, M. H., Luan, X. & Painter, O. Optical transduction and routing of microwave phonons in cavity-optomechanical circuits. *Nat. Photonics* **10**, 489 (2016).
47. Blais, A., Huang, R.-S., Wallraff, A., Girvin, S. M. & Schoelkopf, R. J. Cavity quantum electrodynamics for superconducting electrical circuits: an architecture for quantum computation. *Phys. Rev. A* **69**, 062320 (2004).
48. Devoret, M. H., Wallraff, A. & Martinis, J. M. Superconducting qubits: a short review. Preprint at https://arxiv.org/abs/cond-mat/0411174 (2004).
49. Houzet, M., Serniak, K., Catelani, G., Devoret, M. H. & Glazman, L. I. Photon-assisted charge-parity jumps in a superconducting qubit. *Phys. Rev. Lett.* **123**, 107704 (2019).
50. Glazman, L. I. & Catelani, G. Bogoliubov quasiparticles in superconducting qubits. *SciPost Phys. Lect. Notes* 31 (2021).
51. Siddiqui, A., Olsson, R. H. & Eichenfield, M. Lamb wave focusing transducer for efficient coupling to wavelength-scale structures in thin piezoelectric films. *J. Microelectromech. S.* **27**, 1054 (2018).
52. Chen, Y. et al. Qubit architecture with high coherence and fast tunable coupling. *Phys. Rev. Lett.* **113**, 220502 (2014).
53. Geller, M. R. et al. Tunable coupler for superconducting xmon qubits: perturbative nonlinear model. *Phys. Rev. A* **92**, 012320 (2015).
54. Zeuthen, E., Schliesser, A., Taylor, J. M. & Sørensen, A. S. Electrooptomechanical equivalent circuits for quantum transduction. *Phys. Rev. Appl.* **10**, 044036 (2018).
55. Satzinger, K. J. et al. Quantum control of surface acoustic-wave phonons. *Nature* **563**, 661 (2018).
56. Mirhosseini, M., Sipahigil, A., Kalaee, M. & Painter, O. Superconducting qubit to optical photon transduction. *Nature* **588**, 599–603 (2020).
57. Nguyen, C. T. et al. An integrated nanophotonic quantum register based on silicon-vacancy spins in diamond. *Phys. Rev. B* **100**, 165428 (2019b).
58. Eichenfield, M., Chan, J., Camacho, R. M., Vahala, K. J. & Painter, O. Optomechanical crystals. *Nature* **462**, 78 (2009a).
59. Schmidt, M. K., Poulton, C. G. & Steel, M. J. Acoustic diamond resonators with ultrasmall mode volumes. *Phys. Rev. Res.* **2**, 033153 (2020).

60. Comsol multiphysics®v. 5.4, COMSOL AB, Stockholm, Sweden. www.comsol.com (2020).
61. Eichenfield, M., Chan, J., Safavi-Naeini, A. H., Vahala, K. J. & Painter, O. Modeling dispersive coupling and losses of localized optical and mechanical modes in optomechanical crystals. *Opt. Express* **17**, 20078 (2009b).
62. Safavi-Naeini, A. H. et al. Electromagnetically induced transparency and slow light with optomechanics. *Nature* **472**, 69 (2011).
63. Chan, J. et al. Laser cooling of a nanomechanical oscillator into its quantum ground state. *Nature* **478**, 89 (2011).
64. MacCabe, G. S. et al. Nano-acoustic resonator with ultralong phonon lifetime. *Science* **370**, 840 (2020).
65. Mouradian, S. L. et al. Scalable integration of long-lived quantum memories into a photonic circuit. *Phys. Rev. X* **5**, 031009 (2015).
66. Wan, N. H. et al. Large-scale integration of artificial atoms in hybrid photonic circuits. *Nature* **583**, 226 (2020).
67. Eichenfield, M. & Olsson, R. H. Design, fabrication, and measurement of RF IDTs for efficient coupling to wavelength-scale structures in thin piezoelectric films. In *2013 IEEE International Ultrasonics Symposium (IUS)*. 753–756 (IEEE, 2013).
68. Becker, J. N. et al. All-optical control of the silicon-vacancy spin in diamond at millikelvin temperatures. *Phys. Rev. Lett.* **120**, 053603 (2018).
69. Hensen, B. et al. Loophole-free Bell inequality violation using electron spins separated by 1.3 kilometres. *Nature* **526**, 682 (2015).
70. Farfurnik, D. et al. Optimizing a dynamical decoupling protocol for solid-state electronic spin ensembles in diamond. *Phys. Rev. B* **92**, 060301 (2015).
71. Christle, D. J. et al. Isolated electron spins in silicon carbide with millisecond coherence times. *Nat. Mater.* **14**, 160 (2015).
72. Sukachev, D. D. et al. Silicon-vacancy spin qubit in diamond: a quantum memory exceeding 10 ms with single-shot state readout. *Phys. Rev. Lett.* **119**, 223602 (2017).
73. Bersin, E., Walsh, M., Mouradian, S. L., Trusheim, M. E., Schröder, T. & Englund, D. Individual control and readout of qubits in a sub-diffraction volume. *npj Quantum Inf.* **5**, 1 (2019).
74. Neuman, T., Trusheim, M. & Narang, P. Selective acoustic control of photon-mediated qubit-qubit interactions. *Phys. Rev. A.* **101**, 052342 (2020).
75. Mølmer, K. & Sørensen, A. Multiparticle entanglement of hot trapped ions. *Phys. Rev. Lett.* **82**, 1835 (1999).
76. Sørensen, A. & Mølmer, K. Quantum computation with ions in thermal motion. *Phys. Rev. Lett.* **82**, 1971 (1999).
77. Leibfried, D. et al. Toward heisenberg-limited spectroscopy with multiparticle entangled states. *Science* **304**, 1476 (2004).
78. Matlab®v. R2019b, the MathWorks, Inc., Natick, Massachusetts, United States. www.mathworks.com (2020).
79. Neuman, T., Esteban, R., Giedke, G., Schmidt, M. K. & Aizpurua, J. Quantum description of surface-enhanced resonant raman scattering within a hybrid-optomechanical model. *Phys. Rev. A* **100**, 043422 (2019).

ACKNOWLEDGEMENTS

This material is based upon work supported by the U.S. Department of Energy, Office of Science, Basic Energy Sciences (BES), Materials Sciences and Engineering Division under FWP ERKCK47 (T.N., M.T., P.N., and D.E. - Award 4000183826) 'Understanding and Controlling Entangled and Correlated Quantum States in Confined Solid-state Systems Created via Atomic Scale Manipulation'. The authors (T.N., M.T., P.N.) acknowledge the 'Photonics at Thermodynamic Limits' Energy Frontier Research Center funded by the U.S. Department of Energy, Office of Science, Office of Basic Energy Sciences under Award Number DE-SC0019140 that supported computational approaches used here. D.E. acknowledges partial support from a Bose Research Fellowship. D.E. acknowledges support from Brookhaven National Laboratory, which is supported by the U.S. Department of Energy, Office of Basic Energy Sciences, under Contract No. DE-SC0012704. D.E. acknowledges partial support from NTT Research Inc. P. N. is a Moore Inventor Fellow supported by the Gordon and Betty Moore Foundation. This work is based upon work supported by the U.S. Department of Energy, Office of Science, Advanced Scientific Computing Research (ASCR) under FWP 19-022266 (M.E. and L.H.) 'Quantum Transduction and Buffering Between Microwave Quantum Information Systems and Flying Optical Photons in Fibers'. M.E. performed this work, in part, at the Center for Integrated Nanotechnologies, an Office of Science User Facility operated for the U.S. Department of Energy (DOE) Office of Science. M.E. and L.H. were supported by the Laboratory Directed Research and Development program at Sandia National Laboratories, a multimission laboratory managed and operated by National Technology and Engineering Solutions of Sandia, LLC., a wholly owned subsidiary of Honeywell International, Inc., for the U.S. Department of Energy's National Nuclear Security Administration under Contract No. DE-NA-003525. This paper describes objective technical results and analysis. Any subjective views or opinions that might be expressed in the paper do not necessarily represent the views of the U.S. Department of Energy or the United States Government.

AUTHOR CONTRIBUTIONS

T.N., implemented the numerical model for quantum transduction and performed the calculations. M.T. contributed to the development of the theoretical models. M.E. and D.E. conceived of the phonon-spin cavities. M.E. and L.H. performed the finite-element modeling. D.E., M.E., and P.N. coordinated the project. All authors contributed to the writing of the text, discussed the results and reviewed the final manuscript. T.N., M.E., and M. T. contributed equally to this work.

COMPETING INTERESTS

The authors declare no competing interests.

ADDITIONAL INFORMATION

Supplementary information The online version contains supplementary material available at https://doi.org/10.1038/s41534-021-00457-4.

Correspondence and requests for materials should be addressed to P.N. or D.E.

Reprints and permission information is available at http://www.nature.com/reprints

Publisher's note Springer Nature remains neutral with regard to jurisdictional claims in published maps and institutional affiliations.